Effective Enhancement of TiO$_2$ Photocatalysis by Synergistic Interaction of Surface Species: From Promoters to Co-catalysts

Mario J. Muñoz-Batista, Anna Kubacka,* and Marcos Fernández-García*

Instituto de Catálisis y Petroleoquímica, CSIC, Marie Curie 2, 28049 Madrid, Spain

S *Supporting Information*

ABSTRACT: The enhancement of TiO$_2$-based catalyst activity by effect of surface species is analyzed in the photoelimination of toluene in a complex, ternary system having ceria and Mn-modified carbon nitride in contact with a major anatase phase. With a combination of kinetic and spectroscopic tools applied to the ternary system and corresponding binary/single references, this study delineated a method to quantitatively analyze the quantum yield or reaction rate through a strict measurement of the effect of each component of the ternary system in the generation of the active OH-related radical species of the reaction and the subsequent influence in photocatalytic observables. Using this procedure, the study allows elucidating the role and significance of the surface species in the reaction and, in particular, the important and unique role of a cationic Mn species in modifying the behavior of the carbon-containing species, a fact exclusively occurring in the ternary system and not in the corresponding parent binary/single ones. The method unveils a transformation of such surface species role from that of a promoter to that of a co-catalyst through the synergistic/cooperative interaction of all present phases at the catalyst and establishes a general scheme to measure and interpret the interaction of components in multicomponent photocatalysts.

KEYWORDS: *anatase, ceria, carbon nitride, toluene, degradation, EPR, photoluminescence*
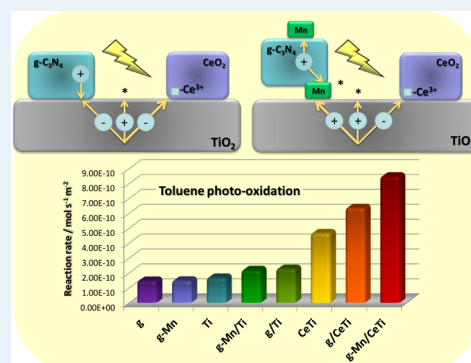
1. INTRODUCTION

Nanopowdered semiconductor materials are customarily used in photocatalysis due to their relatively high surface area available for chemical steps. Nanotitania oxide corresponds to the universal photocatalytic system due to its chemical versatility, high activity, and low cost.[1−4] However, the small primary particle size of all semiconductor particles brings several inherent drawbacks. The first is that the interfacial space charge and band bending that tends to separate electrons and holes will not be present when the dimensions of the crystal are comparable to the width of the depletion layer. The second is that the photogenerated electrons and holes are spatially confined in close proximity. These two issues make electron−hole pairs more likely to recombine without reacting in small particles than in large particles. The third potential disadvantage is that the reaction products are also produced in close proximity (on the surface of the small particle), and this makes the back reaction of intermediate chemical species more likely. This is particularly important in specific reactions such as those involved in the water splitting process. In combination, these three features can lead to important efficiency limitations in nanopowdered materials.[2,3,5−9]

Good photocatalysts balance the increase in density of reaction sites for high surface area powders with mechanisms to mitigate the above-mentioned deleterious effects. A significant number of pathways have been explored to achieve this goal.[1−4] Among them, a generally fruitful path consists of separating electron and hole charge carriers and the subsequent surface reduction and oxidation steps at physically different places of the catalyst. This general strategy has naturally led to composite catalysts. Use of internal electric fields as the main driving force to favor the above-mentioned separation of charge and subsequent reaction steps is connatural to this strategy and has been frequently expressed through binary systems, metal−semiconductor or p−n semiconductor junctions being most popular.[2−4,7−15]

More complex systems, such as ternary ones, are however receiving attention in recent dates. In such complex systems, optimization of charge handling and subsequent chemical steps resulting from the rational design of the components and the hierarchical contact(s) among the existing phases appear as unavoidable requirements for obtaining highly active materials.[2−4] Most common examples in which the building up of a hierarchical multiphase system was successfully accomplished would correspond to the metal-oxide system with a third component such as sulfides, halides, or carbon-containing species. In such materials, the metal, Pt, Au, or Ag, is typically a shuttle component to send or receive charge carriers or to provide effective recombination centers spatially separated from reaction centers located mostly (although not exclusively) at the oxide component.[2,4,11,13,15−17] Additional highly active, multiphasic systems are also encountered when selective

deposition of electron and hole-capturing phases is carried out at different surfaces of a single semiconductor phase.[18] Nonetheless, significant drawbacks of these systems are typically the use of expensive components, such as noble metals, as well as relatively complicated synthesis procedures.

In this contribution we combine a dominant (by weight percentage) anatase component with two nonexpensive semiconductors of different chemical nature. The first is cerium oxide, obtained in a single pot procedure with the main titania phase. The contact between ceria and titania is known to provide rather active materials.[19] It has been applied for the elimination of organic pollutants through reduction and/or oxidation reactions[20−29] and, very recently, for the inactivation of microorganisms.[27,29] The ceria component will handle electron-related species in our system. The second is the g-C_3N_4 carbon nitride. Similarly to the previous case, the combination with titania has shown to provide good photochemical activity in hydrogen production[30,31] or CO_2 reduction,[32] as well as a series of degradation reactions concerning several pollutants.[33−39] It will be introduced in the system with a simple procedure (impregnation) to minimally disturb the binary Ce−Ti system. However, as this material would be the key component to physically localize hole-related species, the most critical charge carrier to generate chemistry,[1,2,4] we will promote the contact with the presence of Mn surface species at the g-C_3N_4 carbon nitride phase. This will take place in a synthetic step prior to its introduction to the ternary system. Important to note is that these two (carbon nitride and cerium) surface species provide (if used separately) maximum activity enhancement of anatase for relatively low weight content, limiting potentially deleterious shadowing effects related to light absorption and/or accessibility to chemical active sites at the major titania component.[20−39] The low weight percentage required for positive boosting of activity facilitates, on the other hand, an easy design of the ternary system in which the contact among carbon and cerium surface species is almost null.

To provide a deep understanding of the system, a full analysis of the kinetically relevant steps of the reaction mechanism together with the identification of the radical active species was carried out using a spectrokinetic approach with the help of several spectroscopic tools including electron paramagnetic resonance (EPR) as well as photoluminescence spectroscopy. With this we quantitatively analyze the quantum yield of the photocatalytic oxidation of toluene, a demanding reaction,[40,41] and provide a strict measure of the effect of each component in the generation of the active radical species and the subsequent influence/control of catalytic observables. Moreover, we delineated the excess functions measuring the synergistic effects occurring between the dual combination of the carbon- and cerium-containing surface species. Using this procedure, we elucidated the important and unique role of Mn in modifying the behavior of the carbon-containing component in the generation and handling of the catalytically active radical species. Such alteration is so profound that can be understood only if such a component alters the role of such a phase from that of a promoter in the binary system to that of a co-catalyst in the ternary system. The study is completed with a multitechnique examination of the catalysts using X-ray diffraction (XRD), X-ray photoelectron spectroscopy (XPS), and infrared and EPR as well as high-resolution electron spectroscopy (HR-TEM).

2. MATERIALS, METHODS, AND MODELING DETAILS

2.1. Catalyst Preparation. Materials were prepared using the microemulsion preparation method. n-Heptane (Scharlau) as organic media, Triton X-100 (Aldrich) as surfactant, and hexanol (Aldrich) as cosurfactant were used. A TiO_2 reference sample was obtained as a first step using titanium tetraisopropoxide (Aldrich) as precursor. In the $CeO_2−TiO_2$ and CeO_2 reference, cerium nitrate (Alfa Aesar) was introduced in the aqueous phase of a microemulsion. After 30 min of agitation, a stoichiometric quantity of tetramethylammonium hydroxide (TMAH) to obtain 2.5% of Ce (III) hydroxide was introduced from the aqueous phase of a similar microemulsion. After 5 min, titanium tetraisopropoxide was introduced into the previously resulting microemulsion drop by drop from a mixture with isopropanol (2:3). Water/(Ti+Ce) and water/surfactant molar ratios were 110 and 18 for all samples, respectively.[42,43] The resulting mixture was stirred for 24 h and centrifuged, and the separated solid precursors were rinsed with methanol and dried at 110 °C for 12 h. After drying, the solid precursors were subjected to a heating ramp (2 °C min^{-1}) to 500 °C, maintaining this temperature for 2 h.

To obtain the graphitic carbon nitride (g-C_3N_4) modified with Mn, the Mn precursor salt (manganese(II) chloride tetrahydrate, Aldrich) was dissolved in deionized water to produce a 10 mM solution. Then, the salt precursor solution was added to 200 mL of a 0.5 mg mL^{-1} uniformly dispersed g-C_3N_4 aqueous solution. The graphitic carbon nitride was obtained previously by calcination of melamine (Aldrich) at 580 °C with a heating ramp of 5 °C min^{-1} for 4 h. The above mixture was kept under stirring for 1 h at room temperature. Afterward, the reaction mixture was centrifuged and washed with deionized water followed by drying at 60 °C.

The incipient wetness impregnation method was used to obtain the g-C_3N_4/TiO_2, g-C_3N_4/$CeO_2−TiO_2$, g-$C_3N_4−MnO_xOH_y$/TiO_2, and g-$C_3N_4−MnO_xOH_y$/$TiO_2−CeO_2$ composite samples. For this, the appropriate amount of g-C_3N_4 or g-$C_3N_4−MnO_xOH_y$ was suspended in methanol and sonicated for 1 h, deposited on the corresponding composite sample, and dried at 110 °C for 24 h. Sample names are Ti, Ce, CeTi, g-Mn, and g for the TiO_2, CeO_2, $CeO_2−TiO_2$, g-$C_3N_4−MnO_xOH_y$, and g-C_3N_4 materials and g/Ti, g-CeTi, g-Mn/Ti, and g-Mn/CeTi for the g-C_3N_4/TiO_2, g-C_3N_4/$CeO_2−TiO_2$, g-$C_3N_4−MnO_xOH_y$/TiO_2, and g-$C_3N_4−MnO_xOH_y$/$TiO_2−CeO_2$, respectively.

2.2. Experimental Techniques. The Brunauer−Emmett−Teller (BET) surface areas and average pore volumes and sizes were measured by nitrogen physisorption (Micromeritics ASAP 2010). XRD profiles were obtained with a Seifert D-500 diffractometer using Ni-filtered Cu Kα radiation with a 0.02° step and fitted using the Von Dreele approach to the Le Bail method;[44] particle sizes and microstrain were measured with XRD using the Williamson−Hall formalism.[45] UV−vis transmission or diffuse-reflectance spectroscopy experiments were performed with a Shimadzu UV2100 apparatus using, for diffuse experiments, $BaSO_4$ as a reference.

TEM analysis of the materials was carried out with a JEOL 2100F TEM/STEM microscope. X-ray energy dispersive spectra (XEDS) analysis was performed in STEM mode, with a probe size ~1 nm, using the INCA x-sight (Oxford Instruments) detector. Photoluminescence spectra were measured at room temperature on a fluorescence spectrophotometer (PerkinElmer LS50B).

XPS data were recorded on 4×4 mm^2 pellets, 0.5 mm thick, prepared by slightly pressing the powered materials, which were outgassed in the prechamber of the instrument at room temperature to a pressure of ca. 2×10^{-8} Torr to remove chemisorbed water from their surfaces. The SPECS spectrometer main chamber, working at a pressure $<10^{-9}$ Torr, was equipped with a PHOIBOS 150 multichannel hemispherical electron analyzer with a dual X-ray source working with Al/Ag Kα (hν = 1486.2 eV) at 120 W, 20 mA using C 1s as energy reference (284.6 eV). Surface chemical compositions were estimated from XP spectra by calculating the integral of each peak after subtraction of the "S-shaped" Shirley-type background using the appropriate experimental sensitivity factors and the CASA-XPS (version 2.3.15) software.

The EPR measurements were done with a Bruker ER200D spectrometer operating in the X band and calibrated with a 2,2-diphenyl-1-picrylhydrazyl (DPPH) standard. For the 5,5-dimethyl-1-pyrroline N-oxide (DMPO) spin-trapping EPR experiments, the samples were suspended in water at a concentration of 0.6 g L^{-1} and sonicated for 4 min. A 0.01 M aqueous solution of the DMPO spin trap (supplied by Sigma) was prepared and kept on ice during the whole set of experiments. Bidistilled water (Elix-10) was employed for these preparations. The solid suspension (100 μL) and the DMPO solution (100 μL) were mixed into an EPR flat quartz cell under atmospheric air and irradiated for different times through a spectroscopic Pyrex glass filter with a cutoff at ca. 220 nm. The cell was then immediately transferred to the spectrometer cavity for EPR analysis. A small decay of the radical concentration (ca. 5% on average) was observed in the dark during the course of spectrum recording. The spectra were obtained at 298 K at a microwave frequency of ca. 9.75 GHz, a microwave power of 19.5 mW, a modulation frequency of 100 kHz, a modulation amplitude of 1 G, and a spectrometer gain of 2×10^5. No significant signal saturation was observed under those conditions. Blank experiments were also performed over mixtures of 100 μL of the DMPO solution and 100 μL of water to confirm the absence of radical formation in the absence of the solid under the employed conditions.

2.3. Photocatalytic Experimental Details. Gas-phase photo-oxidation of toluene (Panreac, spectroscopic grade) was carried in a continuous flow annular photoreactor using a setup described elsewhere (details in the Supporting Information).[46,47] Activity and selectivity for the gas-phase photo-oxidation were tested with ca. 40 mg of the photocatalytic material as a thin layer coating on a Pyrex tube. The corresponding amount of catalyst was suspended in 1 mL of ethanol, painted on a Pyrex tube (cutoff at ca. 290 nm), and dried at room temperature. The reacting mixture (100 mL min^{-1}) was prepared by injecting toluene ($\geq$99%; Aldrich) into a wet (ca. 15–90% relative humidity) 20 vol % O$_2$/N$_2$ flow before entering the photoreactor, yielding an organic inlet concentration of ca. 100–700 ppmv. At the higher end of the organic inlet concentration, the reaction rate shows a zero-order kinetics with respect to the total flow and organic pollutant/oxygen concentrations. After flowing the mixture for ca. 6 h (control test) in the dark, the catalyst was irradiated by four fluorescent UV lamps (Sylvania F6WBLT-65; 6 W, maximum at ca. 350 nm) symmetrically positioned outside the photoreactor. Reaction rates were evaluated (vide supra) under steady-state conditions, typically achieved after ca. 6–10 h from the irradiation starting. No change in activity was detected for all samples within the next 24 h. The

concentration of reactants and products was analyzed using an online gas chromatograph (Agilent GC 6890) equipped with HP-PLOT-Q/HP-Innowax columns (0.5/0.32 mm i.d. × 30 m) and TCD (for CO$_2$ measurement)/FID (organic measurement) detectors. Carbon balance >95% was achieved in all experiments.

2.4. Modeling. *2.4.1. Mass Balance.* To interpret the chemical behavior of the system through a spectrokinetic analysis, we first carried out kinetic experiments with different toluene concentrations, relative humidities, and irradiation levels, using three levels for each factor according to a Box–Behnken design (see details in the Supporting Information Design of Experiments and Figure S1).

According to the photoreactor geometry (see Supporting Information Kinetic Model, where Table S1 shows a simplified reaction scheme of toluene photo-oxidation) and the radiation field (see Radiation Model and particularly Figures S2 and S3), under a kinetic control regimen and taking into account the assumptions (i) the reactor operates under steady state conditions, (ii) the convective flow exists only in the axial coordinate x, (iii) there is negligible axial diffusion when compared to the convective flux in that direction, and (v) there are negligible homogeneous photochemical reactions, toluene mass balance is given by eq 1.[48]

$$v_x(y)\left(\frac{dC_{C_6H_5CH_3}}{dx}\right) = a\, r_{C_6H_5CH_3} \tag{1}$$

The boundary condition necessary to solve this partial differential equation is given by $C_{C_6H_5CH_3}$ ($x = 0$) = $C_{C_6H_5CH_3,\text{in}}$, which is measured experimentally, where $r_{C_6H_5CH_3}$ and $C_{C_6H_5CH_3}$ (in, relative to the inlet concentration) are the average reaction rate and concentration of toluene, respectively. Also, a, $v_x(y)$, and y are the external catalytic surface area per unit volume, the axial velocity profiles (defined for flow between two parallel plates in reference),[49] and the axial coordinate, respectively.

To evaluate the kinetics of the reaction, we used eq 1, where the rate of toluene photo-oxidation must be obtained (see below). The system was solved using MATLAB 2010b. The algorithm use a fifth-order Runge–Kutta subroutine to solve the differential equation coupled to a nonlinear fitting (lsqnonlin; trust-region-reflective algorithm).

2.4.2. Kinetic and Radiation Formulations. To solve eq 1 we thus developed an intrinsic kinetic formulation that takes into account explicitly all chemical and illumination variables above-described. As described in the Supporting Information under our Kinetic Model, the toluene photo-oxidation rate takes the expression presented in eq 2.

$$r_{C_6H_5CH_3} = -\frac{\alpha_1 C_{C_6H_5CH_3} C_{H_2O}}{(1 + K_{H_2O}C_{H_2O})(1 + K_{H_2O}C_{H_2O} + \alpha_2 C_{C_6H_5CH_3})}\sqrt{e^{a,s}} \tag{2}$$

$$\alpha_1 = \frac{k_4 K_{C_6H_5CH_3}[\text{sites}]k_1 K_{H_2O}[\text{sites}]}{\gamma}\sqrt{\frac{\overline{\varphi}}{k_3}} \tag{3}$$

$$\alpha_2 = \frac{k_4 K_{C_6H_5CH_3}[\text{sites}]}{\gamma} \tag{4}$$

Equation 2 includes three parameters: K_{H_2O} is the adsorption constant of water, α_1 and α_1 constants are defined in eqs 3 and 4, and also the local superficial rate of photon absorption ($e^{a,s}(x, y, z)$) at each point of the sample surface, which can be calculated using eq 5 (see the Supporting Information section Radiation Model and Figures S3 and S4 for details).

$$
\begin{aligned}
e^{a,s}(x, y, z) = & \sum_{L=1}^{L=4} \sum_{\lambda} \int_{\varphi_{min}}^{\varphi_{max}} \int_{\theta_{min}}^{\theta_{max}} I_{\lambda,L} \times \exp\left(-\frac{\kappa_{\lambda,gl} e_{gl}}{\cos \beta}\right) \\
& \times \left(1 - \exp\left(-\frac{\kappa_{\lambda,s} e_s}{\cos \beta}\right)\right) \\
& \sin^2 \varphi (n_x \cos \theta + n_y \sin \theta) \, d\varphi \, d\theta \\
& + \sum_{L=1}^{L=4} \sum_{\lambda} \int_{\varphi_{min}}^{\varphi_{max}} \int_{\theta_{min}}^{\theta_{max}} I_{\lambda,L} \\
& \times \exp\left(-\frac{2\kappa_{\lambda,gl} e_{gl} - \kappa_{\lambda,s} e_s}{\cos \beta}\right) \\
& \left(1 - \exp\left(-\frac{\kappa_{\lambda,s} e_s}{\cos \beta}\right)\right) \sin^2 \varphi (n_x \cos \theta \\
& + n_y \sin \theta) \, d\varphi \, d\theta
\end{aligned}
\tag{5}
$$

Note that although $e^{a,s}(x, y, z)$ is obtained at each x,y,z point of the surface, it depends on only two geometrical variables (φ, θ in polar coordinates).

2.4.3. Spectrokinetic Modeling. A insightful combination of kinetic and spectroscopic data can be obtained if we note that the rate between the kinetic parameters (as defined in eq 6) provides almost the same information as a study of the OH$^\bullet$ radical formation using EPR (eq 7; see Supporting Information sections Radiation Model Figures S5 and S6 and EPR Analysis of OH$^\bullet$ Radicals for details concerning the derivation of this equation).

$$
\alpha_k = \frac{\alpha_1}{\alpha_2 K_{H_2O}} = \sqrt{\frac{\bar{\varphi}}{k_3}} k_1 [\text{sites}]
\tag{6}
$$

$$
\alpha_{EPR} = \frac{r[\text{OH}^\bullet]}{\sqrt{e^{a,v}}} = \sqrt{\frac{\bar{\varphi}}{k_3}} k_1 [H_2O]_{ads}
\tag{7}
$$

As discussed below, eqs 6 and 7 can thus render information about the ratio between two elemental steps with kinetic constants k_1 and k_3. According to the kinetic model (summarized in Table S1), step 1 is the creation of hole-related radicals, whereas step 3 accounts for the annihilation of hole-related radicals. Thus, eqs 6 and 7 would generate information about the availability of hole-related radical species during reaction. Confronting these two observables with the reaction rate or quantum yield, we can obtain illumining information about the kinetically relevant species, contrasting at the same time the results using two experimentally independent procedures.[28] Moreover, from the correlation between catalytic observables and those from eqs 6 and 7 and using a simple plotting procedure, we can measure the effect of each component of the catalyst in the generation of the active radical species, thus quantifying numerically its influence in the catalytic behavior.

3. RESULTS AND DISCUSSION

3.1. Characterization Results. The Supporting Information (see Table S2 under Characterization) gives data concerning the chemical composition of the samples. It can be noted that Ce is present in 3 molar % in the corresponding binary/ternary composite samples, whereas Mn is detected only in the g-Mn reference. Considering the percentage at which Mn is present in the g-Mn reference sample (1 molar %), Mn would be well below the detection limit of chemical analysis in the ternary system. In the binary/ternary systems containing carbon nitride, this component is present in a quantity of ca. 1 wt % (0.009 molar %). The physicochemical characterization of the samples is summarized in Table 1. Starting with the surface

Table 1. Main Physicochemical Parameters for the Anatase Phase of the Samples[a]

sample	BET surface area (m^2 g^{-1})	size (nm) TiO$_2$	band gap (eV)
Ti	98.0	12.1	3.20
g/Ti	97.2	12.0	3.12
g-Mn/Ti	98.0	12.4	3.15
CeTi	100.7	13.7	2.97
g/CeTi	101.0	13.4	2.94
g-Mn/CeTi	100.4	13.8	2.96
g-Mn	26.8		2.70
g	26.8		2.70

[a]Standard error: BET, 1.5 m g^{-1}; size, 0.5 nm; ban gap, 0.04 eV.

area, our TiO$_2$ reference presents a value of ca. 98.0 m^2 g^{-1}. This amount modestly increases in the presence of CeO$_2$, whereas the subsequent addition of g-C$_3$N$_4$ does not significantly modify the surface area. If compared with the carbon nitride reference, we thus observed that the surface area is dominated by the major titania component with a rather modest positive effect of CeO$_2$ and a nearly null effect of g-C$_3$N$_4$. Such a situation can be extended to the interpretation of other morphological properties as demonstrated by the pore volume and size values reported in Table S3.

The X-ray diffraction patterns of the composite samples and corresponding single and binary reference systems are shown in Figure 1. Comparison of the patterns makes obvious the exclusive presence of anatase (JCPDS card 78-2486, corresponding to the $I4_1/amd$ space group) in TiO$_2$-based materials. We note that XRD (similarly to Raman, data not shown) does
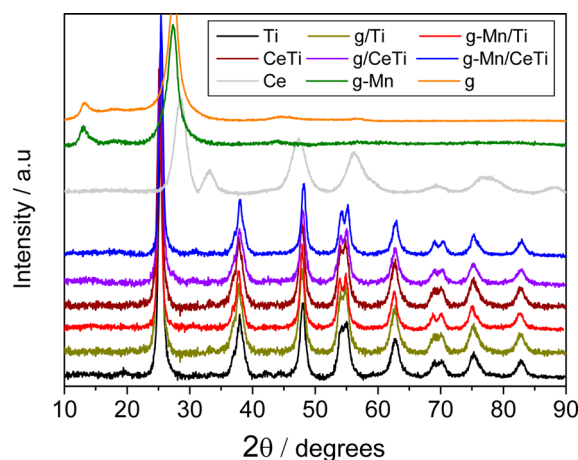
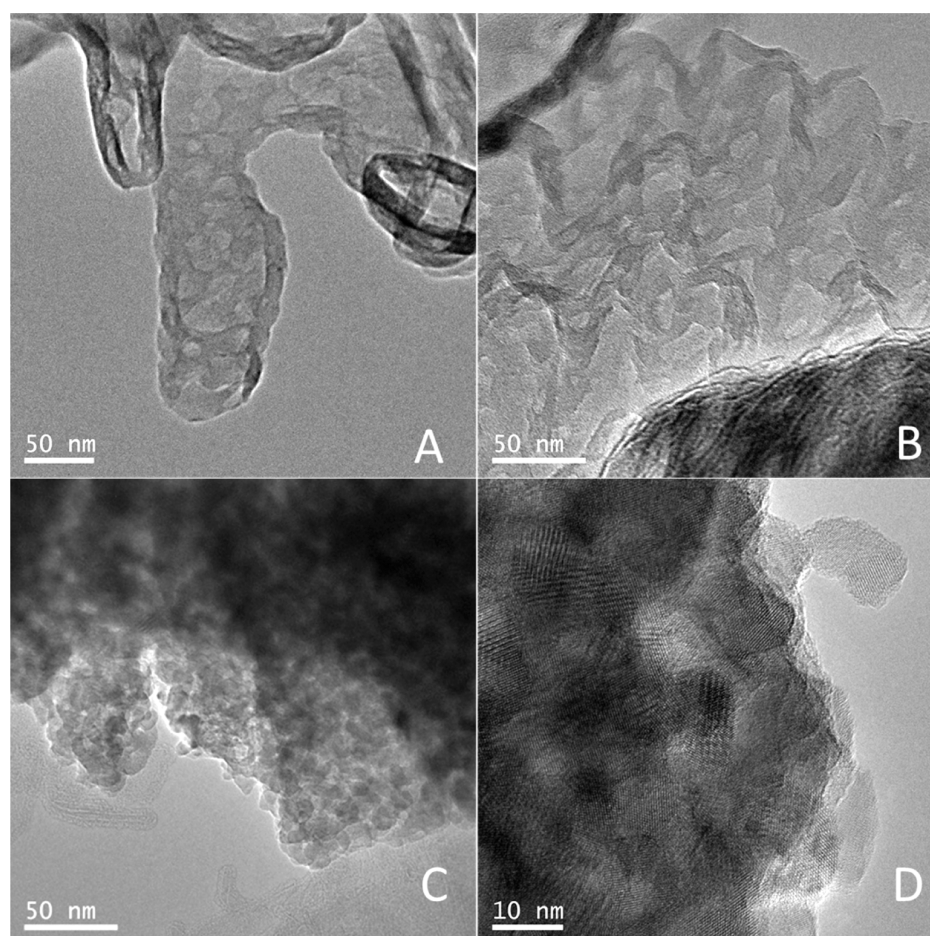**Figure 1.** XRD patterns of the references and samples.

Figure 2. TEM views of (A) g, (B) g-Mn, and (C, D) g-Mn/CeTi samples.

Table 2. Mn, Ce, Ti, and O XPS Fitting Results (Electronvolts) for the Ti, g-Mn, CeTi, g/Ti, g-Mn/Ti, g/CeTi, and g-Mn/CeTi Samples[a]

sample	Mn $2p_{3/2}$	Ce $3d_{3/2}$ (u‴)	Ce $3d_{5/2}$ (v‴)	Ce^{3+}/Ce^{4+}	Ti $2p_{3/2}$	O 1s
Ti					458.1	529.5
g-Mn	641.1					
CeTi		916.6	898.5	0.23	458.3	529.6
g/Ti					458.1	529.4
g-Mn/Ti	nd[b]				458.1	529.5
g/CeTi		916.7	898.5	0.22	458.4	529.7
g-Mn/CeTi	nd	916.6	898.4	0.24	458.2	529.6

[a]Standard error: binding energy, 0.1 eV; species concentration, 5%. [b]nd, not determined (below detection limit).

not provide information about the ceria or carbon nitride components. The state of the two surface species will be analyzed with the help of other techniques (see below).

In consonance with the morphological properties, the anatase structural properties included in Table 1 (i.e., primary particle size) change moderately from TiO_2 and CeO_2–TiO_2 samples and only very modestly in the presence of the carbon nitride component. The similar behavior of all structural and morphological parameters in Tables 1 and S3 is a consequence of the preparation method: whereas the CeO_2–TiO_2 system is produced in a single-pot procedure, the posterior introduction of the carbon nitride using mild conditions does not affect the CeO_2–TiO_2 counterpart. In particular, we note that carbon and or Mn doping of titania/ceria in the TiO_2 or CeO_2–TiO_2 samples does not occur as judged by the constancy of the cell

parameters reported in Table S3 in the Supporting Information. We also note that using Raman (result not shown) we did not detect significant quantities of MnO_x cluster surface species deposited at titania (or ceria).

To further progress in the analysis of the morphology of the samples and to visualize the interaction between the components, a TEM study of the materials is presented in Figure 2. Figure 2A,B micrographs correspond to the g and g-Mn references, whereas Figure 2C,D micrographs concern the g-Mn/CeTi sample. The g-Mn reference displays its characteristic laminar structure without the appearance of any Mn-related cluster or nanoparticle. Considering now the g-Mn/CeTi sample, in Figure 2 we can observe the dominant (titania) oxide component. All around the sample EDXS indicates the simultaneous presence of C/N, whereas its presence is more

straightforwardly observed in Figure 2C at the periphery of the main oxidic part. Thus, the TEM/EDXS combination illustrates the close contact between the carbon nitride and main oxide components both at the periphery and also at any point of the surface of the ceria−titania component. Moreover, as the ceria is a minor component in CeO_2−TiO_2, the g-C_3N_4 is expected to be dominantly in contact with titania. In fact, the EDXS study indicates that this is the case as the Ti signal is correlated only with the N one.

The chemical effects of the TEM-detected interaction between components, more concretely of either ceria or carbon nitride with the dominant titania, were studied using a combination of techniques. Starting with XPS, Table 2 and Figure 3 give a summary of the main experimental and fitting
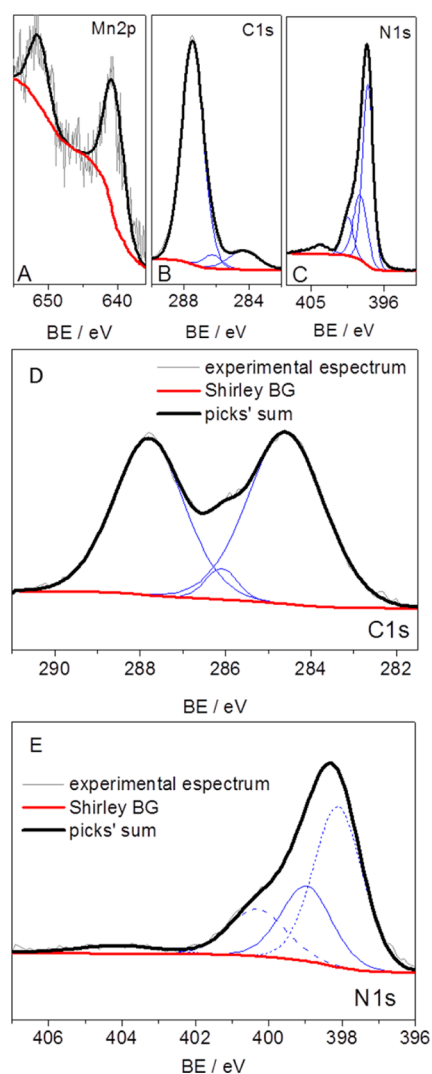

Figure 3. Mn 2p (A), C 1s (B), and N 1s (C) XPS data and fitting results for the g-Mn sample; fitting results for C 1s (D) and N 1s (E) XPS peaks of the g-Mn/CeTi sample.

results for the g-Mn/CeTi sample and reference samples. The table shows no important differences between the g-Mn/CeTi sample and all single and binary references at the Ce 3d, Ti 2p, and O 1s peaks, indicating the low chemical influence of the carbon nitride in the oxidic components. This is a direct consequence of the preparation method used. XPS analysis, the most significant technique providing structural and electronic

information on the ceria component, indicated the importance of interface effects between ceria and titania, which yielded a rather high Ce(III)/Ce(IV) atomic ratio of ca. 3.2 (see ref 28 for further details in the case of the CeTi binary reference system). We stress that Table 2 provides conclusive evidence that ceria behavior is, as expected, not significantly affected by the incorporation of the carbon nitride to the ternary catalyst.

The XPS information about the g and g-Mn components concerns, in the first place, the C 1s and N 1s peaks illustrated in Figure 4. The fitting results of Figure 4 (Tables 3 and 4)
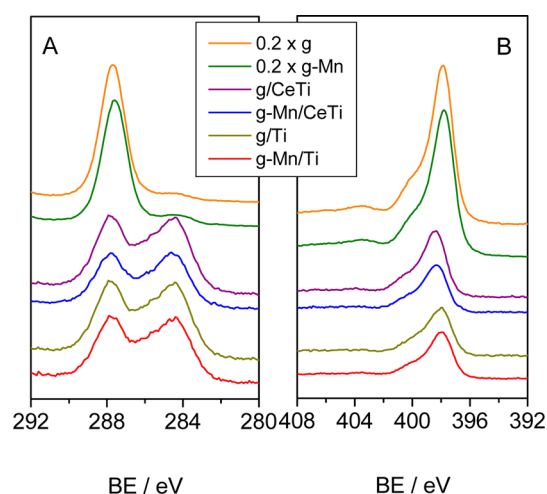
Figure 4. C 1s (A) and N 1s (B) XPS spectra for the g, g-Mn, g/Ti, g-Mn/Ti, g/CeTi, and g-Mn/CeTi samples.

Table 3. C 1s XPS Binding Energies (Electronvolts) and Percentages of the Different Chemical Species Detected for the g, g-Mn, g-Ti, g-Mn/Ti, g/CeTi, and g-Mn/CeTi Samples[a]

sample	C 1s					
	C−C	%	(C)$_3$-N	%	C−N−C	%
g	284.6	10.1	286.2	7.3	287.6	82.6
g-Mn	284.6	11.2	286.2	6.0	287.6	82.8
g/Ti	284.6	53.2	286.1	3.6	287.8	43.2
g-Mn/Ti	284.6	52.2	286.1	3.4	287.8	43.9
g/CeTi	284.6	54.0	286.1	3.4	287.8	42.6
g-Mn/CeTi	284.6	51.6	286.2	3.2	287.8	45.2

[a]Standard error: binding energy, 0.1 eV; species concentration, 5%.

support the conclusion that most important differences are detected in the C 1s and, more exactly, when compared with the g and g-Mn references and other samples including the g-Mn/CeTi catalyst. Three components were observed at the C 1s XPS signal. As previously reported by others in similar systems, the C−C contribution shows the larger variation as a consequence of the different importance of the spurious carbon-containing entities.[50,51] The other C 1s contributions exclusively ascribable to carbon nitride structural moieties, for example, bridging carbons between aromatic moieties (C_3−N) or at the aromatic rings (N−C−N), are also included in Table 3.[35,50,51] They are reasonably constant through the samples having TiO_2 as dominant component. This indicates the rather minor differences in terms of the carbon nitride component among such samples. This observation is also sustained by the N 1s results reported in Figure 4 and Table 4, with limited

Table 4. N 1s XPS Binding Energies (Electronvolts) and Percentages of the Different Chemical Species Detected for the g, g-Mn, g-Ti, g-Mn/Ti, g/CeTi, and g-Mn/CeTi Samples[a]

	N 1s							
sample	π-exc	%	N−H	%	(C)$_3$-N	%	C−N−C	%
g	403.4	5.1	400.6	13.7	399.2	25.7	397.7	55.5
g-Mn	403.8	5.1	400.5	12.4	398.9	26.1	398.0	56.4
g/Ti	404.0	4.9	400.3	15.6	398.9	25.8	398.1	53.7
g-Mn/Ti	404.0	5.0	400.3	15.1	398.9	25.5	398.1	54.4
g/CeTi	403.9	5.4	400.2	12.5	399.1	24.3	398.3	57.8
g-Mn/CeTi	403.9	5.3	400.4	15.6	398.7	25.2	398.1	53.9

[a]Standard error: binding energy, 0.1 eV; species concentration, 5%.

variations among all samples. We additionally corroborated the chemical similitude of the carbon nitride component in all samples studied using infrared spectroscopy (Figure S7 in the Supporting Information).

XPS also rendered information about Mn in the g-Mn reference sample. The Mg 2p peak displays a binding energy of 641.1 eV (Table 2). This observable is compatible with two oxidation states. Mn^{2+} would be compatible with the presence of an oxo-hydroxide species, whereas Mn^{3+} would be compatible with a pure oxidic environment.[52] To describe without doubt the oxidation state and environment of Mn we use EPR. Figure S8 in the Supporting Information indicates the absence of detectable Mn signals in g-Mn due to the similar signal obtained in the presence or absence of the cation. The EPR spectra shown in Figure S8 are characteristic of the pure g-C$_3$N$_4$ material.[53] The result allows inferring the absence of Mn^{2+} ions (paramagnetic in both low- and high-spin states)[54] at the carbon nitride samples. Therefore, the XPS signal should be ascribed exclusively to Mn^{3+} entities in a dominant oxidic environment.

Optical properties and particularly photon absorption are of capital importance to interpret photocatalytic behavior. Figure 5 shows the diffuse reflectance UV−vis spectra of the samples.
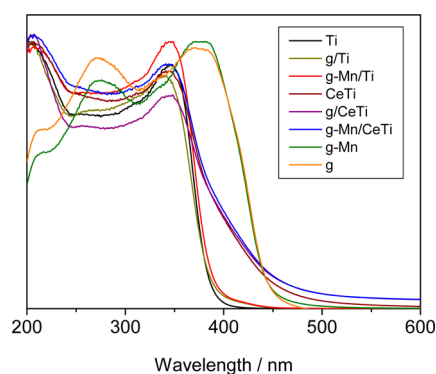

Figure 5. UV−vis spectra of the references and samples.

The samples present a spectrum profile dominated by the titania component, displaying the characteristic intensity decay for a band gap energy of ca. 3.2 eV (Table 1). The spectrum is well differentiated from the g and g-Mn references as they show their characteristic lower band gap energy of 2.7 eV (Table 1).[51] The presence of CeO$_2$ in the Ce−Ti-containing samples slightly decreases (ca. 0.23 eV) the band gap and modifies the spectrum shape in the visible region (Figure 5). The effect of ceria at the band gap energies of CeTi, g/CeTi, and g-Mn/CeTi systems is mostly attributable to a quantum size effect (or effects)[55] at the anatase phase[55] due to the complete absence of

doping effects (as suggested by the XRD analysis) as well as the rather modest presence (3 molar %) of ceria. The rough opposite trend of anatase particle size and band gap energy (Table 1) does suggest the dominance of primary particle quantum size effects.[55] The subsequent addition of the g-C$_3$N$_4$ component does not alter light absorption properties and band gap energy in g/CeTi and g-Mn/CeTi. Rather modest changes below 0.03 eV are thus presented in Table 1. This would indicate that the absorption properties are dominated by titania with a modest contribution originated by the surface species present at the anatase surface and, particularly, from the CeO$_2$ component.

The combined use of microscopy and spectroscopic tools gives thus a complete structural picture of the carbon nitride and ceria species at the titania surface and measures the electronic effects on all components. We see a minimum distortion of the ceria and carbon nitride components from the corresponding binary systems to the two (g/CeTi, g-Mn/CeTi) main systems. The two parent binary systems (g/Ti, CeTi) were previously described in detail elsewhere.[28,35]

3.2. Analysis of Photocatalytic Properties. A representative example of the performance in toluene photo-oxidation for ternary samples and reference materials is presented in Figure 6. The reaction rate per unit surface area is relatively low
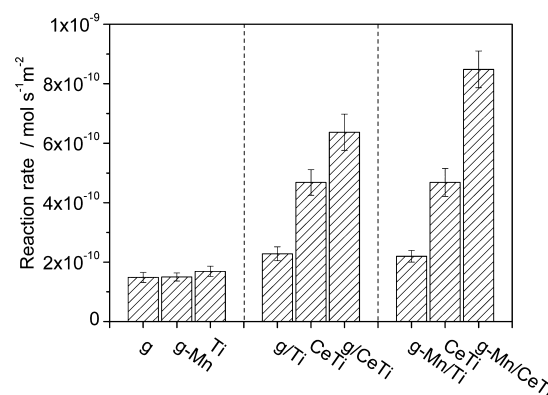

Figure 6. Surface-area-normalized reaction rate for toluene photo-oxidation (C_0 = 700 ppm, relative humidity = 70%, T = 30 °C).

for all simple reference systems, g, g-Mn, and Ti. Interestingly, the association of Mn with the carbon nitride does not display significant enhancement of activity, despite Mn being known to handle holes,[18,31] and thus would favor separation of charge in this specific system. More interestingly, comparison of g/CeTi and g-Mn/CeTi with their respective binary reference systems, which consider the contact of the dominant titania component with the other two, allows a different enhancement effect in the

absence/presence of Mn to be distinguished. Whereas in g/CeTi we observed an almost additive effect and thus a promoter-like behavior of ceria and carbon nitride without interference among them, in g-Mn/CeTi a strong synergistic or cooperative effect among components appears evident in the photoactivity.

To interpret such a complex chemical behavior, we utilize the spectrokinetic analysis of the photo-oxidation reaction to numerically quantify the different contributions to the photocatalytic activity. Our main focus is the numerical interpretation of the activity as a sum of different contributions ascribable to the binary ceria–titania and carbon nitride–titania and/or cooperative effects. To this end, kinetic experiments free of external/internal diffusion problems (see the Supporting Information section Kinetic Experiments and External and Internal Mass Transfer Limitations and Table S4 and S5) were carried out in combination with an analysis of radical species produced during the photoexcitation of the materials.

Toluene photodegradation has been shown to be a hole-triggered reaction in TiO$_2$-based photocatalysts.[28,56−58] We first analyze this issue quantitatively with the help of EPR (see the Supporting Information section EPR Analysis of OH$^\bullet$ Radicals). A comparison of the initial rate of OH$^\bullet$ for the first minutes (before multiple additions, within consecutive reactions, of OH$^\bullet$ radicals to the spin trapping molecule would drive to the formation of diamagnetic species) is customarily used to compare the sample power to generate this radical species.[59−62] The EPR measurements provide the slope of the dotted straight lines presented in Figure 7, proportional to the corresponding rates of OH$^\bullet$ formation.[61,63] After a normalization that takes into account the optical properties, this renders the observable described by eq 7.
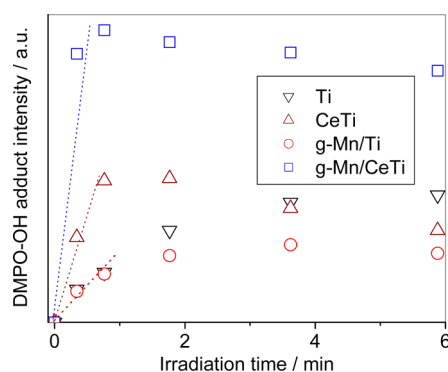
Figure 7. Time evolution of the DMPO−OH radical intensities in the presence of the different catalysts.

The kinetic study experimental (circles) and fitting (surfaces) results according to eq 1 are presented in Figure 8. This figure also includes a comparison of the reactor outlet toluene concentration measured and the corresponding outcome of the fitting procedure as a measure of the goodness of the fit (Figure 8A). The fitting is rather good with a maximum root-mean-square error of 2.3%. Values for the kinetic parameters used in solving eqs 1 and 2 are presented in Table 5. As previously mentioned in the discussion of eq 6, the kinetic parameters can render (as the EPR study did) information about the initial steps of the reaction. Numerical comparison of values obtained from eqs 6 and 7 is shown in Table 6. In this table the values have been normalized by a constant to allow an easy

comparison between them (see text concerning units of these observables in Table 6).

The analysis of the reaction rate (Figure 9) or true quantum yield (Supporting Information Figure S9) as a function of the two measurements rendered by eqs 6 and 7 would be thus used to disentangle effects in the ternary complex system. Observing the trends presented in the above-mentioned figures, we first point out that the parallel evolution of the two observables clearly demonstrates that trends in the catalytic properties through the sample series are dominated by the common factor to eqs 6 and 7, that is, the $k_1/(k_3)^{1/2}$ ratio. As detailed previously, this is a consequence of the key role played by hole-related species in the kinetically relevant step(s) of the reaction.[28] Note that eqs 6 and 7 also contain the primary quantum yield as a common factor, but the use of a UV excitation together with the presence of the same dominant titania absorber in all samples makes this factor reasonably constant through the series of samples analyzed. We can highlight, on the other hand, the point that although both equations give the same qualitative answer, the error propagation (Table 6) is significantly less affecting the EPR results due to the simpler experimental/mathematical procedure to obtain it. Despite this, the two methods provide the same qualitative answer in Figures 9 and S9, mutually serving as validation tests for each other.

Focusing on the analysis of the different contributions to the catalytic properties, a simple function of the ternary system can be defined with respect to the main reference (Ti) and the parent binary systems (eq 8).

$$X(\text{g-Mn/CeTi; ideal})$$
$$= X(\text{Ti}) + \nabla(X(\text{g-Mn/Ti}) - X(\text{Ti}))$$
$$+ \nabla(X(\text{CeTi}) - X(\text{Ti})) \qquad (8)$$

X is a physical observable, particularly a catalytic property such as the reaction rate or the quantum yield. This equation intends to allow to quantitative measurement if the interaction between the surface species present in the g-Mn/CeTi catalyst is detrimental, positive but simply additive, or, as expected in a good photocatalyst, synergistic. The difference between the $X(\text{g-Mn/CeTi; ideal})$ and the real observable corresponds to an "excess" function, which can be negative, zero, or positive. When applied simultaneously to two physical quantities, as in Figures 9 and Supporting Information Figure 9 is applied to a couple corresponding to a catalytic property (either the reaction rate or the quantum yield) and the kinetic or EPR observable(s), we end up in a correlation plot to interpret the physical ground of the catalytic behavior. Furthermore, to provide a more complete picture, the outcome of the correlation plot analysis and, particularly, the implications in charge separation and annihilation will be interpreted with the additional help of photoluminescence spectroscopy.

In Figures 9 and S9, the sum described by eq 8 is presented as a graphical result in a squared box. The correlation plot points corresponding to the ideal result of the couples activity/"kinetic" and activity/"EPR" appear far from the real measurements. The corresponding excess functions are included as numerical values in the plots. The measurement indicates that the "catalytic" excess function is positive and would correspond to ca. 60−70%. This excess function is quantitatively justified by the enhancement in OH-related radicals as measured with EPR (see the numerical values included in Figures 9 and S9). The
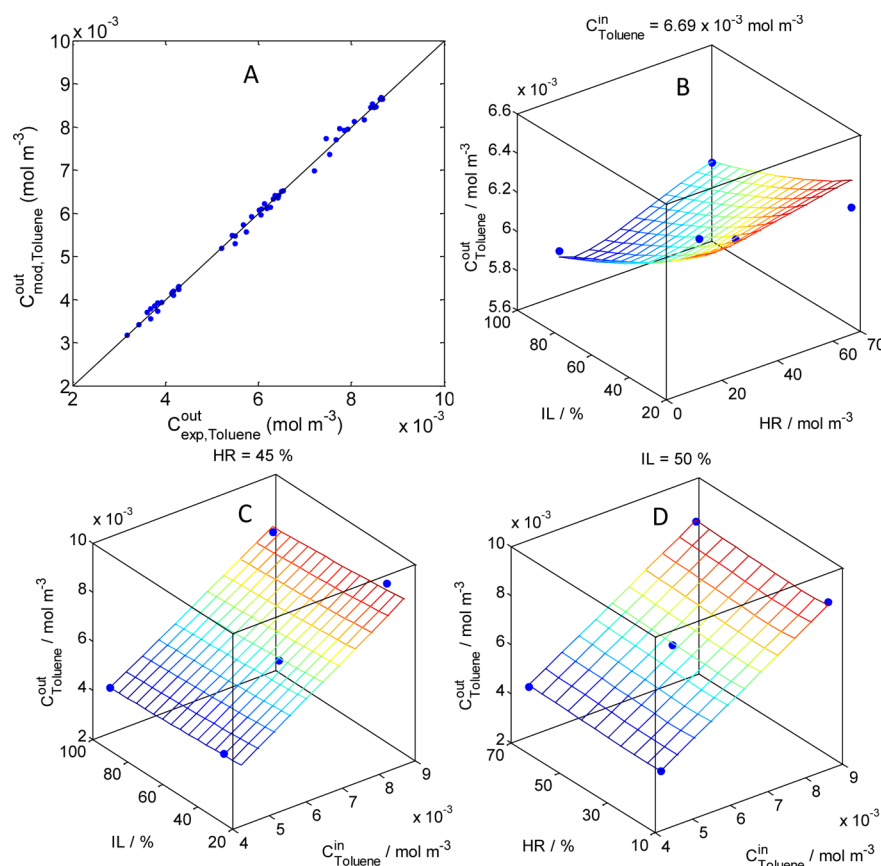
Figure 8. (A) Toluene experimental and model prediction concentration outlet; (B−D) model (surface) and experimental result (point) for g-Mn/CeTi sample. IL, irradiation level; HR, relative humidity; $C_{Toluene}^{in}$ and $C_{Toluene}^{out}$, initial and final toluene concentrations, respectively; mod and exp, relative to model and experimental values, respectively.

Table 5. Kinetic Parameters[a]

	Ti	g-Mn/Ti	CeTi	g-Mn/CeTi
α_1	1.6×10^{-4}	1.9×10^{-4}	2.5×10^{-4}	3.9×10^{-4}
α_1 error	0.4×10^{-4}	0.5×10^{-4}	0.9×10^{-4}	1.0×10^{-4}
α_2	8.4×10^{2}	6.2×10^{2}	4.0×10^{2}	3.9×10^{2}
α_2 error	2.5×10^{2}	1.5×10^{2}	1.2×10^{2}	1.3×10^{2}
K_{H_2O}	8.6	8.0	7.3	7.1
K_{H_2O} error	2.9	2.4	2.5	3.0
RMSE		2.3		

[a]Units: α_1 (einstein$^{-1/2}$ s$^{-1/2}$ m$_{sup}^{-1}$ (m$_{air}^3$)^2); α_2 (mol$_{Tol}$/m$_{air}^3$), K_{H_2O} (mol$_{H_2O}$/m$_{air}^3$). RMSE (%), root-mean-square error.

Table 6. Values of α_k- and α_{EPR}-Normalized Parameters[a]

	Ti	g-Mn/Ti	CeTi	g-Mn/CeTi
α_k (au)	0.23	0.38	0.87	1.39
α_k error	0.11	0.17	0.50	0.82
α_{EPR} (au)	0.35	0.35	0.93	1.50
α_{EPR} error	0.09	0.09$_5$	0.11	0.15

[a]Normalization parameters: α_k 1.0×10^7 (mol$_{Tol}$ einstein$^{-1/2}$ s$^{-1/2}$ m$_{sup}^{-1}$)$^{-1}$; α_{EPR} 6.0×10^{-3} (spin(OH$^\bullet$) einstein$^{-1/2}$ s$^{-1/2}$ m$^{-3/2}$)$^{-1}$.

same analytical procedure can be applied to the g/CeTi system and the adequate reference binary systems, g/Ti and CeTi. As shown in Figure S10 in the Supporting Information, for this ternary system there is roughly (within experimental error) an additive effect in the photocatalytic activity, again sustained by a similar effect in the formation of OH-related radicals.
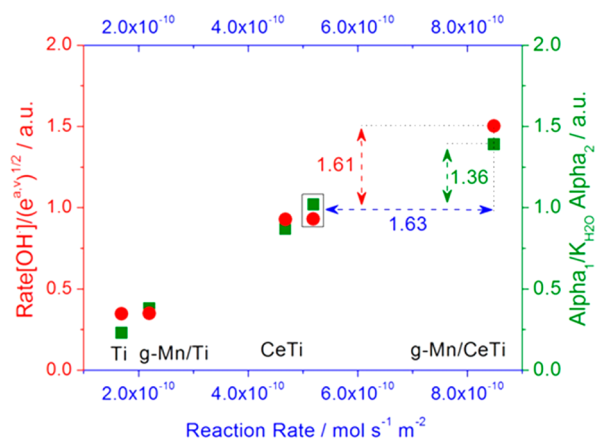

Figure 9. Correlation plot of the kinetic parameter ratio and the normalized rate of OH-related radical formation versus the reaction rate for the Ti, CeTi, g-Mn/Ti, and g-Mn/CeTi samples. Symbols in the square frame show values for an ideal ternary system. See text for details.

According to eq 7 and previous discussions, the similar behavior of the observables in the parity plot of Figure 9 is thus driven by the $k_1/\sqrt{k_3}$ ratio or, in other words, by a combination of the production and annihilation of the hole-related charge carrier species. Before further discussing this point with the help of photoluminescence spectroscopy, we stress the fact that the procedure just described allows the chemical/catalytic effects produced by the two surface species present at the main

titania component to be quantified. From a chemical point of view, the relevant outcome is that the addition of a relatively small quantity of Mn to the carbon nitride component transforms the combination of the two species present at the titania surface from roughly additive to synergistic.

The photoluminescence properties of the samples under UV excitation are presented in Figure 10. Starting first with the
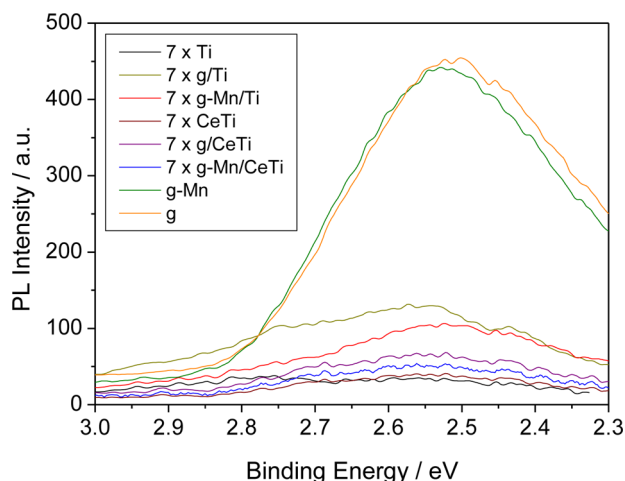

Figure 10. Photoluminescence spectra of the references and samples. λ_{ext} = 280 nm. Note the scale factors of Ti, CeTi, g/Ti, g/CeTi, g-Mn/Ti, and g-Mn/CeTi samples.

main titania component, we note that above 2.0 eV the photoluminescence of titania samples displays the presence of two or three peaks.[64−66] Additional low-energy peaks are less important to generate photochemistry and always related to the presence of defective Ti (interstitial or lattice) states.[67] The peaks about 2.0 eV can be grouped in two types of transitions corresponding to high-energy (sometimes called green) and low-energy (red) de-excitation channels. Although we lack a definitive interpretation of the photoluminescence spectra of anatase materials, the first transition mostly probes de-excitation of excited electrons in localized (typically oxygen-related) states that annihilates with trap-related holes, whereas the second probes the de-excitation of electron-localized states with holes at the valence band.[64−66] In the binary g-Ti and CeTi systems, the photoluminescence properties are significantly modified from the main titania component. In both cases new de-excitation channels, inherent to the binary (and not the single) components, have been observed in our previous works.[29,35] For the carbon nitride this de-excitation channel withdraws electrons for titania and annihilates them with holes from the carbon nitride (increasing photoluminescence signal with respect to tiania), whereas in the presence of ceria, electrons from titania are captured at the ceria−titania interface by anion vacancies (decreasing photoluminescence signal with respect to titania). Despite the different chemical natures of the surface species and as sketched in Scheme 1A, both species essentially favor the capture of electrons from TiO_2 with involvement of anion vacancies in the case of ceria and an annihilation process in the case of the carbon nitride.[29,35,68] A simple look at Figures 6, 9, and Figure S9 indicates that ceria plays such a role more efficiently (a fact depicted in Scheme 1 as a ticker line for the corresponding charge species).

In the binary g/Ti system the strong luminescence of the carbon nitride component dominates the spectrum even for

Scheme 1. Schematic Representation of the Main Charge Carrier Handling Events (Lines) either Related to Charge Recombination through Hetero-junctions Concerning Two Components of the Catalyst or Used in Kinetically Relevant Chemical Steps[a]
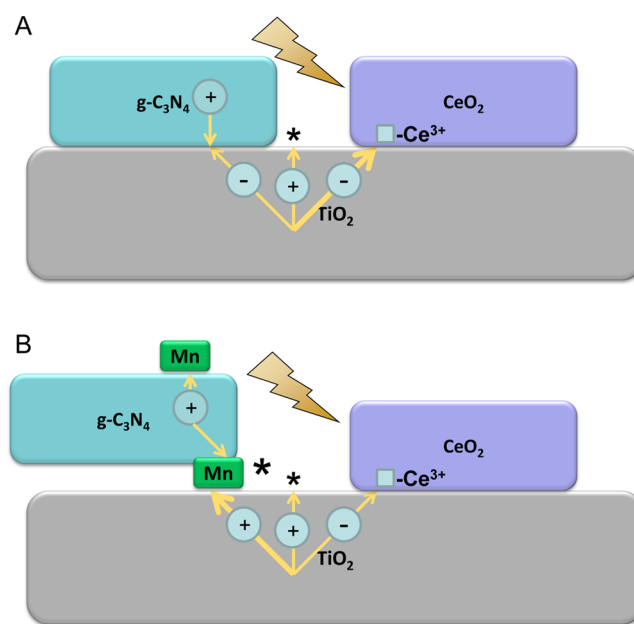
[a]All other charge production/handling events are omitted for simplicity. Asterisks represent surface active sites in photo-oxidation of toluene (A) in the g/CeTi system and (B) in the g-Mn/CeTi system. See text for details.

low contents, rendering higher photoluminescence intensity with respect to the pure Ti reference material.[35] The role of the carbon nitride in contact with Ti is strongly altered in the presence of Mn, which now depletes the intensity of the photoluminescence signal in g-Mn/Ti with respect to g/Ti. A similar situation is encountered when the g-Mn/CeTi and g/CeTi sample results are compared (Figure 10). This situation will happen only if a new charge handling center occurs in the presence of Mn.

In the absence of Mn the two species (carbon nitride and ceria) present at the titania surface behave independently, with significant similarity with the corresponding parent binary system's photocatalytic behavior. On the other hand, and as illustrated in Scheme 1B, the presence of a hole-related managing species (Mn) provides a beneficial modification of the charge handling properties of the system (photoluminescence results indicating decreasing recombination, Figure10) and, more concretely, favors the production of hole-related radicals (EPR result, Figure 7) by facilitating the physical separation of electrons and holes of the main titania component. Moreover, it opens an additional path to use additional hole-related radicals produced at the carbon nitride component for chemistry, contrarily to the case of the parent binary system. Note that this occurs, as discussed under Characterization Results, without practical physicochemical alterations of any of the components of the ternary system, at least when compared with the corresponding binary reference materials.

The modification of the charge handling properties through a mediator, Mn species (present in a minute proportion at the g-Mn/CeTi ternary catalyst, i.e., 1×10^{-2} mol %) creates a new

center for hole availability at a physically separated location than the main electron-handling one, the former being located at the carbon nitride—Mn—titania interface and the latter being located at the ceria—titania interface (Scheme 1). This is achieved using two common components, carbon nitride and ceria oxide, and a relatively simple preparation procedure that does not require nanoengineering tools and/or expensive (noble metal) components. The physical separation of the two charge carrier handling sites at the titania surface together with the potential of carbon nitride holes to be involved in chemical steps can be interpreted as a change of the role of this component from a promoter to a co-catalyst as the toluene elimination is known[28,56−58] to be (as also demonstrated here) a hole-driven reaction. The activity enhancement observed for g-Mn with respect to the g reference sample would indicate that the second pathway for hole production, exclusively ascribable to the carbon nitride phase (i.e., without participation of the titania component), may have relatively minor chemical consequences with respect to the one concerning the main titania component. In passing, we note that the charge handling center previously described as the carbon nitride—Mn—titania interface is a simplification of the real situation; clearly Mn is at the core of the hole localization and handling, and the close relationship with the titania surface is required for effectively using such species in subsequent chemical steps. Whether this happens in a single site or requires several sites as described in titania-based systems by Majima and co-workers is to be analyzed.[69] To end the discussion, we note that the formation of a high active, ternary system with physical separation of electron and hole-related charge carrier species can be generalized to most of the degradation photocatalytic reactions concerning organic compounds as they are also hole-driven reactions.[1−4] This shows the potential of the system in photodegradation reactions.

4. CONCLUSIONS

In this contribution we report a novel method to analyze the photocatalytic behavior of complex, ternary systems in terms of the physicochemical and catalytic relevance of each component. Specifically, the method allows measuring quantitatively if the interaction between the components in a catalyst is detrimental, positive but simply additive, or, as expected in a good photocatalyst, synergistic and interprets this in relation to the formation of the kinetically relevant radical species involved in the photo-oxidation process. Thus, the method establishes a general scheme to measure and interpret through physico-chemical roots the interaction of components in a multi-component or composite photocatalyst.

Such a method is applied here to a TiO_2 anatase-based photocatalyst having ceria and carbon nitride species at its surface. Combined with a multitechnique (XRD, XPS, IR, EPR, UV—visible, photoluminescence) characterization of the ternary sample and binary/single reference compounds, it uncovers a unique role of Mn cationic species incorporated at the surface of the carbon nitride component. Exclusively in the ternary system and, therefore, in the simultaneous presence of ceria and anatase, we show the creation of a new Mn-related center for hole-related handling species with kinetic significance in the photo-oxidation of toluene. Creation of such a center confers the role of a co-catalyst to the carbon nitride component at the same time that it allows a physical separation of charge carriers at the whole system, leading to a significant boost of the photocatalytic activity in a TiO_2-based ternary system born

form a singular and unique synergistic interaction between two surface species.

■ ASSOCIATED CONTENT

ⓢ Supporting Information

The following files are available free of charge on the ACS Publications website at DOI: 10.1021/cs501408u.

> Kinetic and radiation model used, as well as details concerning experimental design, internal/external mass diffusion limitations, EPR measurements, catalyst characterization and photocatalytic results (PDF).

■ AUTHOR INFORMATION

Corresponding Authors
*(A.K.) Fax: (+34915854760). E-mail: ak@icp.csic.es.
*(M.F.-G.) Fax: (+34915854760). E-mail: mfg@icp.csic.es.

Notes
The authors declare no competing financial interest.

■ REFERENCES

(1) Vinu, R.; Madras, G. *J. Indian Inst. Sci.* **2010**, *90*, 189−230 09704140.
(2) Kubacka, A.; Colon, G.; Fernandez-Garcia, M. *Chem. Rev.* **2012**, *112*, 1555−1614.
(3) Jing, L.; Zhou, W.; Tian, G.; Fu, H. *Chem. Soc. Rev.* **2013**, *42*, 9509−9549.
(4) Wang, Z.; Liu, Y.; Huang, B.; Dai, Y.; Lou, Z.; Wang, G.; Xhang, X.; Qin, X. *Phys. Chem. Chem. Phys.* **2014**, *16*, 2758−2774.
(5) Albery, W. J.; Philip, N. B. *J. Electrochem. Soc.* **1984**, *131*, 315−325.
(6) Serpone, N.; Lawless, D.; Khairutdinov, R. *J. Phys. Chem.* **1995**, *99*, 16555−165564.
(7) Tachikawa, T.; Fujitsuka, M.; Majima, T. *J. Phys. Chem. C* **2007**, *111*, 5259−5275.
(8) Osterloh, F. E. *Chem. Mater.* **2008**, *20*, 35−54.
(9) Kudo, A.; Miseki, Y. *Chem. Soc. Rev.* **2009**, *38*, 253−278.
(10) Lin, X.; Xing, J.; Wang, W.; Shan, Z.; Xu, F.; Huang, F. *J. Phys. Chem. C* **2007**, *111*, 18288−18293.
(11) Augugliaro, V.; Yurdakal, L.; Loddo, V.; Palmisano, G.; Palmisano, L. *Adv. Chem. Eng.* **2009**, *20*, 1−35.
(12) Primo, A.; Garcia, H.; Corma, A. *Phys. Chem. Chem. Phys.* **2011**, *13*, 886−910.
(13) Kamat, P. V. *J. Phys. Chem. Lett.* **2012**, *3*, 663−672.
(14) Wang, W.; Huang, X.; Wu, S.; Zhou, Y.; Wang, L.; Shi, H.; Liang, Y.; Zou, B. *Appl. Catal. B: Environ.* **2013**, *134−135*, 293−301.
(15) Yang, J.; Wang, D.; Han, H.; Li, C. *Acc. Chem. Res.* **2013**, *46*, 1900−1909.
(16) Kudo, A. *Pure Appl. Chem.* **2007**, *79*, 1917−1934.
(17) Zhang, H.; Zhu, Y. *J. Phys. Chem. C* **2010**, *114*, 5822−5830.
(18) Li, R.; Zhang, F.; Wang, D.; Yang, J.; Li, M.; Zhu, J.; Zhou, X.; Han, H.; Li, C. *Nature Comm.* **2013**, *4*, 1432−1436.
(19) Zou, M.; Kong, Y.; Wang, J.; Wang, Q.; Wang, W.; Wang, B.; Fan, P. *Spectrochim. Acta, Part A* **2013**, *101*, 82−90.
(20) Parasupree, S.; Suzuki, Y.; Prisa-Art, S.; Yoshikawa, S. *J. Solid State Chem.* **2005**, *178*, 128−134.

(21) Tong, T.; Zhang, J.; Tian, B.; Chen, F.; He, D.; Anpo, M. *J. Colloid Interface Sci.* **2007**, *315*, 382−388.

(22) Li, G.; Zhang, D.; Yu, Y. C. *Phys. Chem. Chem. Phys.* **2009**, *11*, 3775−3782.

(23) Stengl, V.; Bakardejieva, S.; Murafa, N. *Mater. Chem. Phys.* **2009**, *114*, 217−226.

(24) Lin, H.; Wang, M.; Wang, Y.; Liang, Y.; Cao, W.; Su, Y. *J. Photochem. Photobiol., A* **2011**, *223*, 157−162.

(25) Wang, Y.; Li, B.; Zhang, C.; Cui, L.; Kang, S.; Li, X.; Zhou, L. *Appl. Catal., B* **2013**, *130−131*, 277−284.

(26) Liu, Y.; Fang, P.; Cheng, Y.; Gao, Y.; Chen, F.; Liu, Z.; Dai, Y. *Chem. Eng. J.* **2013**, *219*, 478−485.

(27) Karunakaran, C.; Gomathisankar, P. *ACS Sustainable Chem. Eng.* **2013**, *1*, 1555−1563.

(28) Munoz-Batista, M. J.; Kubacka, A.; Gomez-Cerezo, M. N.; Tudela, D.; Fernandez-Garcia, M. *ACS Catal.* **2014**, *4*, 63−72.

(29) Munoz-Batista, M. J.; Ferrer, M.; Fernandez-Garcia, M.; Kubacka, A. *Appl. Catal. B: Environ.* **2014**, *154−155*, 350−359.

(30) Yan, H.; Yang, H. *J. Alloys Compd.* **2011**, *509*, L26−29.

(31) Obregon, S.; Colon, G. *Appl. Catal. B: Environ.* **2014**, *144*, 775−783.

(32) Zhou, S.; Liu, Y.; Li, J.; Wang, Y.; Jiang, G.; Zhao, Z.; Wang, D.; Duan, A.; Liu, J.; Wen, Y. *Appl. Catal. B: Environ.* **2014**, *158−159*, 20−29.

(33) Yu, J.; Wang, S.; Low, J.; Xiao, W. *Phys. Chem. Chem. Phys.* **2013**, *15*, 16883−16889.

(34) Miranda, C.; Mansilla, H.; Yanez, J.; Obergon, S.; Colon, G. *J. Photochem. Photobiol., A* **2013**, *253*, 16−24.

(35) Munoz-Batista, M. J.; Kubacka, A.; Fernandez-Garcia, M. *Catal. Sci. Technol.* **2014**, *4*, 2006−2015.

(36) Shidharan, K.; Jang, E.; Park, T. J. *Appl. Catal. B: Environ.* **2013**, *142−143*, 718−723.

(37) Wang, X.-J.; Yang, W.-Y.; Li, F.-T.; Xue, Y.-B.; Liu, R.-H.; Llao, Y.-J. *Ind. Eng. Chem. Res.* **2013**, *52*, 17140−17146.

(38) Boohprokov, N.; Wetchakon, N.; Waxler, D.; Inceesungrom, B. *J. Colloid Interface Sci.* **2014**, *417*, 402−409.

(39) Zhang, L.; Jing, D.; She, X.; Liu, X.; Yang, D.; Lu, Y.; Li, J.; Zheng, Z.; Gou, J. *J. Mater. Chem. A* **2014**, *2*, 2071−2077.

(40) Fuerte, A.; Hernandez-Alonso, M. D.; Maira, A. J.; Martinez-Arias, A.; Fernandez-Garcia, M.; Conesa, J. C.; Soria, J. *J. Catal.* **2002**, *212*, 1−12.

(41) Munoz-Batista, M. J.; Kubacka, A.; Gomez-Cerezo, M. N.; Tudela, D.; Fernandez-Garcia. *Appl. Catal. B: Environ.* **2014**, *156−157*, 307−313.

(42) De Gennes, P. G.; Taupin, C. *J. Phys. Chem.* **1982**, *86*, 2294−2303.

(43) Kubacka, A.; Fernandez-Garcia, M.; Colon, G. *J. Catal.* **2008**, *254*, 272−284.

(44) Le Bail, A.; Duroy, H.; Forquet, J. L. *Mater. Res. Bull.* **1988**, *23*, 447−452.

(45) Williamson, G. K.; Hall, W. H. *Acta Metall.* **1953**, *1*, 22−31.

(46) Kubacka, A.; Bachiller-Baeza, B.; Colon, G.; Fernandez-Garcia, M. *Appl. Catal. B: Environ.* **2010**, *93*, 274−281.

(47) Kubacka, A.; Colon, G.; Fernandez-Garcia, M. *Catal. Today* **2009**, *143*, 286−292.

(48) Imoberdorf, G. E.; Irazoqui, H. A.; Cassano, A. E.; Alfano, O. M. *Ind. Eng. Chem. Res.* **2005**, *44*, 6075−6085.

(49) Bird, R. ; Steward, W. ; Lightfoot, E. *Transport Phenomena*, 2nd ed.; Wiley: New York, 2002; pp 137−245.

(50) Yu, J.; Wang, S.; Low, J.; Xiao, W. *Phys. Chem. Chem. Phys.* **2013**, *11*, 16883−16890.

(51) Dong, G.; Xhang, Y.; Pan, Q.; Qui, J. *J. Photochem. Photobiol. C* **2014**, *20*, 33−50.

(52) Biesinger, M. C.; Payne, B. P.; Grosvenor, A. P.; Lau, L. W. M.; Gerson, A. R.; Smart, R. St. C. *Appl. Surf. Sci.* **2011**, *257*, 2717−2730.

(53) Chen, S.; Hu, Y.; Meng, S.; Fu, X. *Appl. Catal. B: Environ.* **2014**, *150− 151*, 564−573.

(54) Aboukais, A.; Abi-Aad, E.; Taouk, B. *Mater. Chem. Phys.* **2013**, *142*, 564−571.

(55) Fernandez-Garcia, M.; Martinez-Arias, A.; Hanson, J. C.; Rodriguez, J. A. *Chem. Rev.* **2004**, *104*, 4063−4105.

(56) d'Hennezel, O.; Pichat, P.; Ollis, D. F. *J. Photochem. Photobiol., A* **1998**, *118*, 197−204.

(57) Coronado, J. M.; Soria, J. *Catal. Today* **2007**, *123*, 37−41.

(58) Sleiman, M.; Conchon, P.; Ferronato, C.; Chovelon, J.-M. *Appl. Catal., B* **2009**, *86*, 159−165.

(59) Grela, M. A.; Coronel, M. E. J.; Colussi, A. J. *J. Phys. Chem.* **1996**, *100*, 16940−16945.

(60) Janzen, E. G.; Sankuratry, N.; Kotake, Y. *J. Magn. Reson.* **1996**, *111*, 254−262.

(61) Kubacka, A.; Colon, G.; Fernandez-Garcia, M. *Appl. Catal. B: Environ.* **2010**, *95*, 238−244.

(62) Chen, Q.; Shi, H.; Li, W. S.; Xu, Y.; Wu, D. W. *Catal. Sci. Technol.* **2012**, *2*, 1213−1220.

(63) Kubacka, A.; Munoz-Batista, M.; Ferrer, M.; Fernandez-Garcia, M. *Appl. Catal. B: Environ* **2013**, *140−141*, 680−690.

(64) Tachikawa, T.; Majima, T. *J. Am. Chem. Soc.* **2009**, *131*, 8485−8487.

(65) Wang, X.; Feng, Z.; Shi, J.; Jia, G.; Shen, S.; Zhou, J.; Li, C. *Phys. Chem. Chem. Phys.* **2010**, *12*, 7083−7089.

(66) Mercado, C. C.; Seeley, Z.; Bandyopadhyay, A.; Bose, Z.; McHale, J. L. *ACS Appl. Mater. Interface* **2011**, *3*, 2281−2288.

(67) Finnazi, E.; Valentin, C. D.; Pacchioni, G. *J. Phys. Chem. C* **2009**, *113*, 3382−3391.

(68) Jin, Z.; Murakami, N.; Tsubota, T.; Ohno, T. *Appl. Catal. B: Environ.* **2014**, *150−151*, 479.

(69) Park, Y.; Kim, W.; Monllor.Satoca, D.; Tachikawa, T.; Majima, T.; Choi, W. *J. Phys. Chem.. Lett.* **2013**, *4*, 189−194.